

Rapid characterization of complex structural phase transitions using powder diffraction and an area detector

Philip Pattison,^{a*} Kenneth D. Knudsen,^b Radovan Cerny^c and Edmond Koller^d

^aInstitute of Crystallography, University of Lausanne, CH-1015 Lausanne, Switzerland,

^bDepartment of Physics, Institute for Energy Technology, PO Box 40, N-2027 Kjeller, Norway,

^cLaboratory of Crystallography, University of Geneva, CH-1211 Geneva 4, Switzerland, and

^dDepartment of Solid State Physics, University of Geneva, CH-1211 Geneva 4, Switzerland.

E-mail: philip.pattison@ic.unil.ch

(Received 19 November 1999; accepted 16 March 2000)

The use of a high-intensity and well collimated X-ray beam from a third-generation synchrotron source, combined with an area detector with online readout capabilities, allows high-quality powder patterns to be obtained with exposure times of only a few seconds. Powder measurements of a rare-earth manganate perovskite ($\text{Nd}_{0.43}\text{Sr}_{0.57}\text{MnO}_3$) were performed in the temperature range 105–200 K, and the data were of sufficient quality to be able to extract, *via* Rietveld refinement, accurate values for the lattice constants and atomic parameters. The temperature dependence of the Mn–O–Mn bond angles and Mn–O distances obtained in this manner illustrate the well known correlation between the distortion of the MnO_6 octahedra and the onset of orbital ordering. The success of this study, for which only two hours of synchrotron beam time was required, indicates the enormous improvements in efficiency and throughput which area detectors are bringing to powder diffraction experiments.

Keywords: X-ray diffraction; two-dimensional detection; structural phase transitions.

1. Introduction

Perovskites with the general formula $R_{1-x}A_x\text{MnO}_3$ ($x = 0-1$), where R is a rare-earth element and A is a divalent cation, have attracted much attention in recent years due to the unusual behaviour of some of their physical properties. In general, these compounds are electrically insulating and paramagnetic at room temperature, and undergo a transition to a metallic and ferromagnetic (FM) state at the Curie temperature (T_C), typically in the range 200–280 K. Depending on the composition, there may also be a transition to an antiferromagnetic (AFM) state at the Neel temperature (T_N), typically between 120 and 200 K. One intriguing effect is the so-called giant magnetoresistance that takes place when a magnetic field is applied close to T_C in the paramagnetic region, resulting in some cases in a change in electrical resistivity of several orders of magnitude. There are also other potential technological applications of this group of materials, such as electrodes in solid-state fuel cells (*e.g.* $R = \text{La}$, $A = \text{Ca}$) and catalysts (*e.g.* $R = \text{La}$, $A = \text{Sr}$).

One compound in this family, $\text{Nd}_{1-x}\text{Sr}_x\text{MnO}_3$, has been studied extensively as a function both of doping concentration (x) and temperature (T) [see *e.g.* Maezono *et al.* (1998) and Moritomo *et al.* (1998), where the x - T phase diagram is illustrated]. The low-temperature structure below ~ 160 K is metallic and FM up to a concentration of

$x = 0.48$. Between $x = 0.48$ and 0.53 there is a charge-ordered (charge-exchange, CE) AFM phase, and for $x > 0.53$ the charge ordering breaks down and a layer-type (A-type) AFM phase is formed. The charge-ordered phase around $x = 0.5$ has been the subject of particularly intense interest, using X-ray, synchrotron and neutron diffraction techniques. Neutron diffraction measurements by Caignaert *et al.* (1996) at room temperature showed that this compound is an orthorhombically distorted perovskite ($a \simeq 2^{1/2}a_p$, $b \simeq 2a_p$, $c \simeq 2^{1/2}a_p$, where a_p is the lattice constant of the ideal cubic perovskite; $a_p = 3.85$ Å in this case), of symmetry *Imma*. These room-temperature results were subsequently confirmed by high-quality synchrotron powder diffraction measurements (Woodward *et al.*, 1998). The behaviour of the magnetization, resistivity and lattice constants as a function of temperature has been investigated by Kuwahara *et al.* (1995), also for $x = 0.5$. That work revealed a sharp phase transition (FM to CE-AFM) at $T_N = 158$ K, accompanied by large lattice deformations.

In the present work we have investigated the temperature dependence of the structural phase transitions in the doped manganate, $\text{Nd}_{1-x}\text{Sr}_x\text{MnO}_3$, for $x = 0.57$. At this doping concentration we expect to see a transition from the room-temperature paramagnetic phase to a layered A-type AFM phase below ~ 200 K, in accordance with the results of a neutron diffraction study of $\text{Nd}_{1-x}\text{Sr}_x\text{MnO}_3$ with $x = 0.5$ and $x = 0.55$ (Kawano *et al.*, 1997). Our goal was not

only to observe the phase transition but also to perform a full structural analysis at each temperature, in order to confirm the relationship between bond angles and distances in the MnO_6 octahedra and the onset of the AFM phase. The use of a focused synchrotron beam and an area detector allowed us to perform a rapid structural study over a wide temperature range. In this manner we were able to probe the thermal hysteresis common in this type of transition, and already observed in resistivity measurements (Kuwahara *et al.*, 1999). In addition, we were intrigued by reports of a 'phase segregation' or 'phase mixtures' observed during structural transitions in these and related manganates (see *e.g.* Radaelli *et al.*, 1995; Arulraj *et al.*, 1998). During the course of the present study a synchrotron powder diffraction investigation of the same compound (but with $x = 0.5$) was carried out by Woodward *et al.* (1999). It is interesting to note that they also observed a separation into coexisting macroscopic phases at low temperature, and we will make extensive comparison with their work. Each of the powder patterns measured by Woodward *et al.* (1999) took several hours, even when using a linear position-sensitive detector. In contrast, our exposure time per pattern on the image plate was ~ 10 s, albeit with a worse angular resolution. Nevertheless, we will show that it is perfectly feasible to extract all of the interesting structural parameters from our image-plate data.

2. Experimental

Fine-grained powder of $\text{Nd}_{0.43}\text{Sr}_{0.57}\text{MnO}_3$ was obtained by rubbing a commercial target (PRAXAIR Surface Technologies, nominal composition $\text{Nd}_{0.5}\text{Sr}_{0.5}\text{MnO}_3$, raw materials 99.9% purity). The Nd/Sr ratio was determined by

electron-probe microanalysis to be 0.43 (1)/0.57 (1). About 2 mg of the sample was filled into a thin-walled 0.3 mm borosilicate capillary and mounted on a Huber 1004 goniometer head. A reference powder pattern was collected at room temperature between 6 and $60^\circ 2\theta$ and at a wavelength of 0.59716 \AA , making use of the high-resolution powder diffractometer at BM1B (Swiss–Norwegian beamline), installed on a bending-magnet beamline at the ESRF. This diffractometer is equipped with an NaI scintillation counter and an Si[111] analyser crystal, providing intrinsic peak widths as low as 0.01° .

For the study of temperature effects the same sample was mounted on the spindle axis of a commercial image-plate detector system (MAR345) at beamline BM1A at the ESRF. This detector is equipped with an image plate of diameter 345 mm and a selectable pixel size (100 or 150 μm) for the readout. The readout cycle is 80 s (scan plus erase time) using the entire area of the plate and a pixel resolution of 150 μm . Complete powder patterns were collected by exposing the powder sample for 10 s at a wavelength of 0.80027 \AA . A focused beam with a cross section of $0.5 \text{ mm} \times 0.5 \text{ mm}$ was used for the measurements. The focusing is achieved with the combination of an Rh-coated collimating mirror, an Si[111] sagittally focusing double-crystal monochromator, and another Rh-coated mirror for vertical focusing. The sample-to-detector distance was 280 mm, which gave a 2θ range of 0 – 31.6° . The distance and wavelength were calibrated by means of a least-squares refinement of several powder rings of silicon powder, NBS 640b. The sample was cooled by means of a dry nitrogen stream from an Oxford Cryosystem unit. The sample was first cooled down to 105 K and allowed to equilibrate for about 15 min. It was then warmed up to

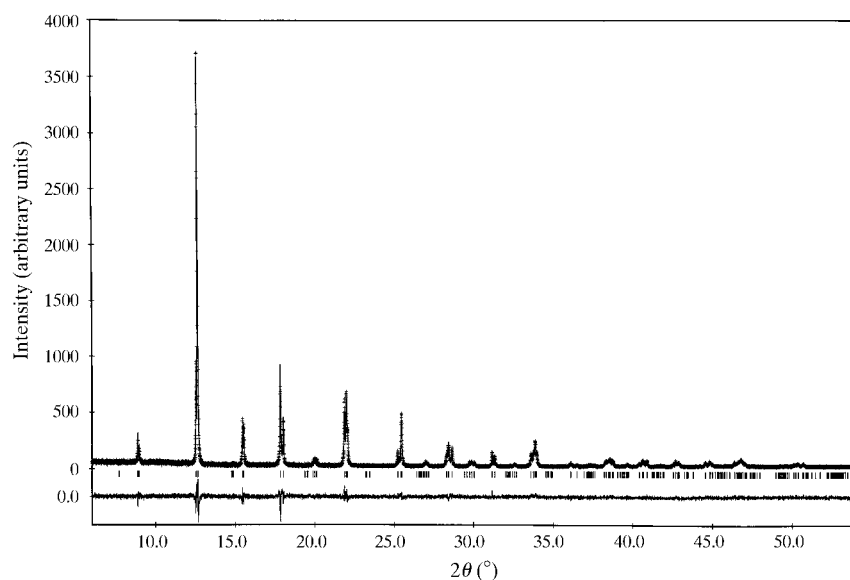


Figure 1

High-resolution powder pattern of $\text{Nd}_{0.43}\text{Sr}_{0.57}\text{MnO}_3$ collected at room temperature. The experimental data points are marked as dots. $\lambda = 0.59716 \text{ \AA}$. Also shown in the figure, as a smooth curve, is the final result from the Rietveld refinement together with the difference curve (observed minus computed intensities).

Table 1

Lattice parameters, atomic coordinates, occupancy and displacement parameters for $\text{Nd}_{0.43}\text{Sr}_{0.57}\text{MnO}_3$ at room temperature based on the high-resolution powder study.

a (Å)	b (Å)	c (Å)	Space group		
5.4273 (1)	7.6275 (2)	5.4702 (1)	<i>Imma</i>		
Atom	x	y	z	Occupancy	U_{iso}
Nd	0.00000	0.25000	−0.0002 (9)	0.425 (9)	0.0087 (2)
Sr	0.00000	0.25000	−0.0002 (9)	0.575 (9)	0.0087 (2)
Mn	0.00000	0.00000	0.50000	1.00000	0.0049 (4)
O _{ax}	0.00000	0.25000	0.457 (3)	1.00000	0.016 (5)
O _{eq}	0.75000	−0.025 (1)	0.25000	1.00000	0.016 (3)

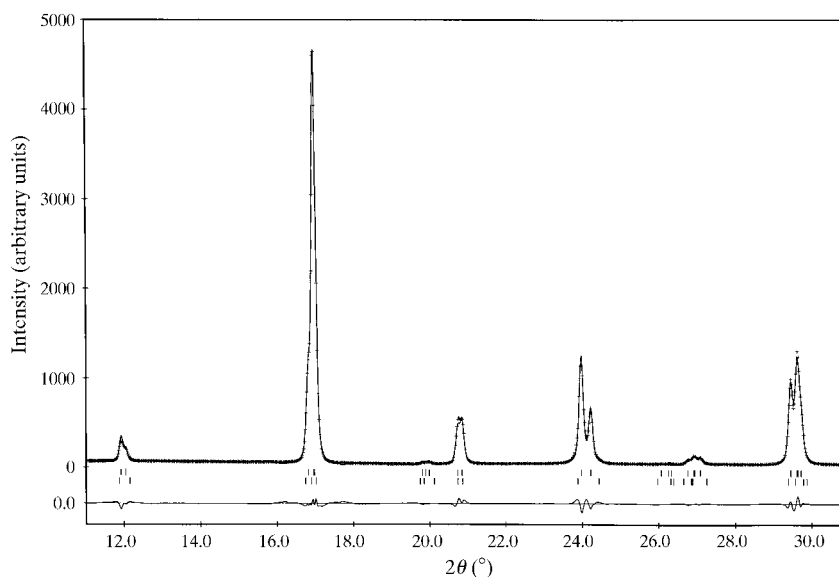
200 K in steps of 5 K as images were collected, and finally cooled down to 105 K, again collecting images at intervals of 5 K. The time lapse between each powder pattern was approximately 3 min, which was mainly to allow the temperature of the cryostream to stabilize.

The two-dimensional images were converted to one-dimensional powder diffractograms by the *FIT2D* program (Hammersley, 1999), after appropriate correction for centre offset and misalignment of the detector plate (values extracted from the calibration with silicon powder). This one-dimensional pattern was subsequently transformed into a format suitable for input to *GSAS* (Larson & Von Dreele, 1987), and Rietveld refinements on each complete powder pattern were performed making use of *GSAS* with a profile function including asymmetry correction (Finger *et al.*, 1994).

3. Results and discussion

The high-resolution reference powder pattern collected at room temperature is shown in Fig. 1. A Rietveld refinement was performed on this pattern, allowing us to extract the lattice parameters, atomic coordinates and displacement parameters, shown in Table 1. The starting values employed for the atomic coordinates were those calculated by Woodward *et al.* (1998) for the $x = 0.5$ compound. The occupancy was refined to Nd/Sr = 0.43/0.57, in good agreement with the results of the electron-probe microanalysis. All peaks were indexed in the space group *Imma*, and there was no evidence of any impurity phase resulting in additional peaks or unusual peak shapes. The refined parameters from the high-resolution room-temperature measurement were used as starting values for the subsequent temperature-dependent study with the image-plate system.

Fig. 2 shows an integrated powder pattern from one exposure (10 s) on the image plate ($T = 200$ K). Fig. 3 shows a selected range of 2θ (23.5 – 25°), which illustrates the drastic structural changes that take place as the temperature is increased from 105 K and upwards. There is clearly a phase transition taking place, with one peak disappearing (23.8°) and others appearing (24.0° and 24.2°). However, the change is not abrupt, but occurs gradually over a temperature range of more than 70 K. The low-temperature phase was found to be of the same *Imma* symmetry as the high-temperature phase, but with a dramatic change in lattice constants. It is possible to observe in Fig. 3 that a small amount of the high-temperature phase still remains

**Figure 2**

Integrated powder pattern of $\text{Nd}_{0.43}\text{Sr}_{0.57}\text{MnO}_3$ collected at $T = 200$ K on the MAR345 image plate. The experimental data points are marked as dots. $\lambda = 0.80027$ Å. The distance between sample and image plate was 280 mm. Pixel resolution = 150 μm . Also shown in the figure, as a smooth curve, is the final result from the Rietveld refinement together with the difference curve. The upper set of tick marks indicate the positions of peaks for the HTO phase, and the lower set indicate the positions where the peaks for the LTO phase are expected (this phase is not present at 200 K).

(small peak at 24.2°) even at 105 K, which was the lowest temperature measured. A complete Rietveld refinement was performed at each temperature, extracting the relative concentrations of each of the two crystallographic phases, and the result showing the coexistence range is given in Fig. 4. We see that above 190 K the system has one phase only, which we will call the HTO (high-temperature orthorhombic) phase following the notation of Woodward *et al.* (1999). At 105 K there is still about 20% of the HTO phase remaining, the rest having transformed to the LTO (low-temperature orthorhombic) phase. It is interesting to note the pronounced hysteresis of the system, which was also observed by Laffez *et al.* (1996) in low-temperature electron diffraction when working with the $x = 0.5$ compound. It is worth addressing the question of why this transition is so broad in temperature. One possibility would be that the transition is actually sharp (first order) on a local level (small domains in the sample), but that different domains have different activation energies for the transition to occur, and therefore produce a broad transition on the macroscopic level. It is very likely that the sharpness of the transition is related to the compositional homogeneity of the sample in question, particularly since float-zone grown crystals of the same nominal composition show abrupt changes in the lattice constants (Kuwahara *et al.*, 1995, 1999).

Other authors have reported ‘phase segregation’ in related systems such as $\text{Nd}_{0.25}\text{La}_{0.25}\text{Ca}_{0.5}\text{MnO}_3$ (Arulraj *et al.*, 1998). The angular resolution of the latter neutron study did not allow an analysis of the different phases. The system was therefore treated as one single average phase which showed a drastic jump in the lattice constants around the transition temperature. The results reported by Woodward *et al.* (1999) for their sample 1 are practically identical to our data for the HTO phase, which is also present in their sample at 20% concentration even at 100 K. However, their LTO phase competes with a further LTM (low-temperature monoclinic) phase, which develops

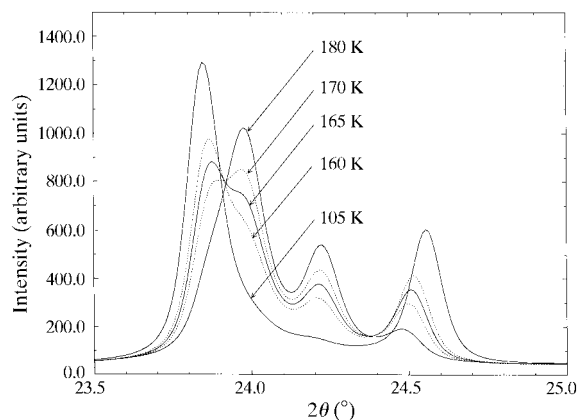


Figure 3

A plot of a selected range of 2θ showing the changes in the powder pattern which take place as the temperature is increased from 105 K. The curves are based on integrated image-plate data.

below ~ 140 K. The LTM phase is identified with the charge-ordered CE-AFM structure, which indeed is only expected to be present in the narrow concentration range $x = 0.48$ – 0.53 . No additional peaks corresponding to the LTM phase could be observed in our results, which is consistent with our dopant concentration of $x = 0.57$.

The results of low-temperature neutron diffraction measurements confirm the presence of a layered AFM phase at a concentration $x = 0.55$ of $\text{Nd}_{1-x}\text{Sr}_x\text{MnO}_3$ (Kawano *et al.*, 1997). The layered character of this phase is well illustrated by the extremely anisotropic resistivity observed in the same compound in single crystals grown by the float-zone technique as observed by Kuwahara *et al.* (1999), who demonstrated that the resistivity in the ac plane is orders of magnitude lower than the resistivity along the axial b direction. We can expect that the onset of the anisotropic orbital ordering will be accompanied by an increase in the orthorhombic distortion, as evidenced by the distortion parameter D . This parameter is defined as $D = \Sigma|a_i - \langle a \rangle|/3a_i$, where a_i is the length of axis i and $\langle a \rangle = (acb^{1/2})^{1/3}$, and indicates the overall distortion from the ideal cubic perovskite lattice. The HTO phase has a distortion of less than 0.5%, and this parameter jumps to above 1% in the LTO phase which appears at 170 K, increasing smoothly to 1.27% as the temperature is lowered to 105 K. Both an expansion in the ac plane and a contraction in the b direction are responsible for this distortion, as can be seen from the lattice constants for both phases shown in Figs. 5(a) and 5(b) for the ac plane and the b direction, respectively. Maezono *et al.* (1998) have calculated the orbital polarization in manganese oxides, and conclude that the degenerate e_g orbitals are preferentially occupied as $d_{x^2-y^2}$ in the layered AFM state (orbital ordering). This leads to the formation of a two-dimensional $x^2 - y^2$ band in the ac plane, which would explain the highly anisotropic electronic properties and the distortion of the

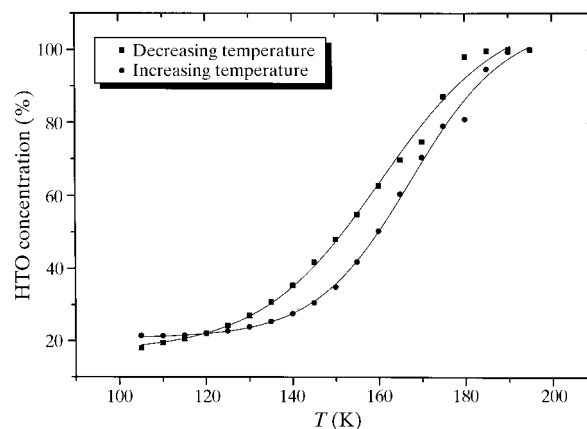


Figure 4

Evolution with temperature of the concentration of the high-temperature phase of $\text{Nd}_{0.43}\text{Sr}_{0.57}\text{MnO}_3$. Each data point represents a complete Rietveld refinement based on two-dimensional powder data collected with the MAR345 image-plate system at the Swiss–Norwegian beamline at a wavelength of 0.80027 \AA .

MnO₆ octahedra. Similar arguments can be found by Woodward *et al.* (1998), who investigated the effect of cation size on the room-temperature structures of the Ln_{0.5}A_{0.5}MnO₃ perovskites.

The atomic coordinates extracted from the Rietveld refinement at different temperatures provide us with the possibility of calculating interatomic distances and angles. Of particular interest is the distortion within the MnO₆ octahedra. Fig. 6(a) shows the relative arrangement of the octahedra in the *ac* plane at a temperature of 200 K. Each Mn atom is surrounded by four equatorial O atoms (O_{eq}) and by two axial O atoms (O_{ax}). Fig. 6(b) shows a view into the *bc* plane, illustrating the relative tilt of the octahedra. In the HTO phase above ~160 K, we find an Mn–O_{eq}–Mn angle of ~168° and a substantially smaller Mn–O_{ax}–Mn angle of ~154°. In the LTO phase below 160 K, the Mn–O_{eq}–Mn angle is almost unchanged at ~166°, while the Mn–O_{ax}–Mn angle increases somewhat to ~157°. These results are almost identical to the Mn–O–Mn bond angles published by Kawano *et al.* (1997) for the float-zone grown crystals of Nd_{0.45}Sr_{0.55}MnO₃.

The influence both of Mn–O–Mn bond angles (octahedral tilt) and Mn–O bond lengths (Jahn–Teller distortion of the octahedra) on the structure of Nd_{1-x}Sr_xMnO₃ has been discussed by Van Veenendaal & Fedro (1999). For the bond angles determined in our case for the LTO phase

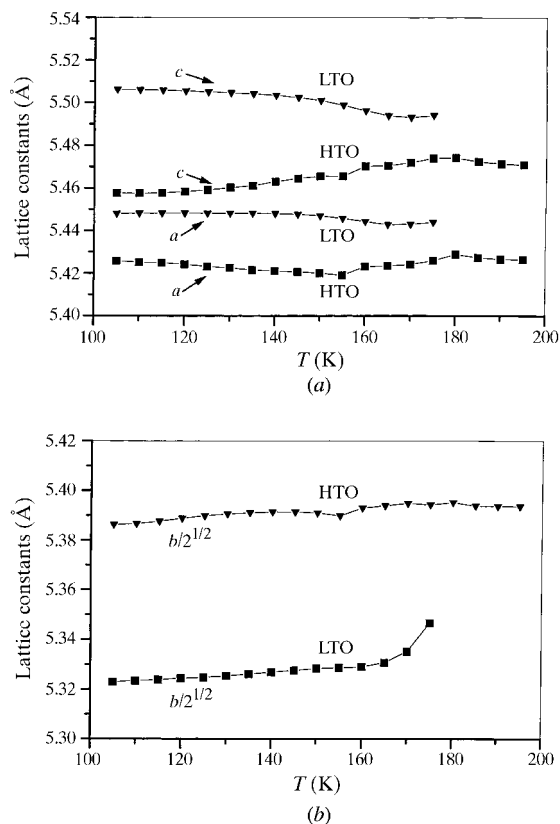


Figure 5
The development of the lattice parameters for the two crystallographic phases over the temperature range studied.

(166° and 157° for *ac* and *b* directions, respectively), they clearly predict the A-AFM as the lowest-energy magnetic structure. Moreover, we observe an Mn–O_{eq} bond length of 1.948 Å, compared with an Mn–O_{ax} bond length of 1.925 Å in the LTO phase. This is direct evidence of the Jahn–Teller distortion, leading to an axial compression of the MnO₆ clusters and hence a further stabilization of the layer-type AFM structure (Van Veenendaal & Fedro, 1999). This axial compression is not present in our temperature-dependent study of the HTO phase, in accordance with the results for the same phase at 160 K reported by Woodward *et al.* (1999). In the room-temperature paramagnetic phase, however, we again observe some axial compression (although not as dramatic as in the LTO phase), in line with the results of Caignaert *et al.* (1996) and Woodward *et al.* (1999).

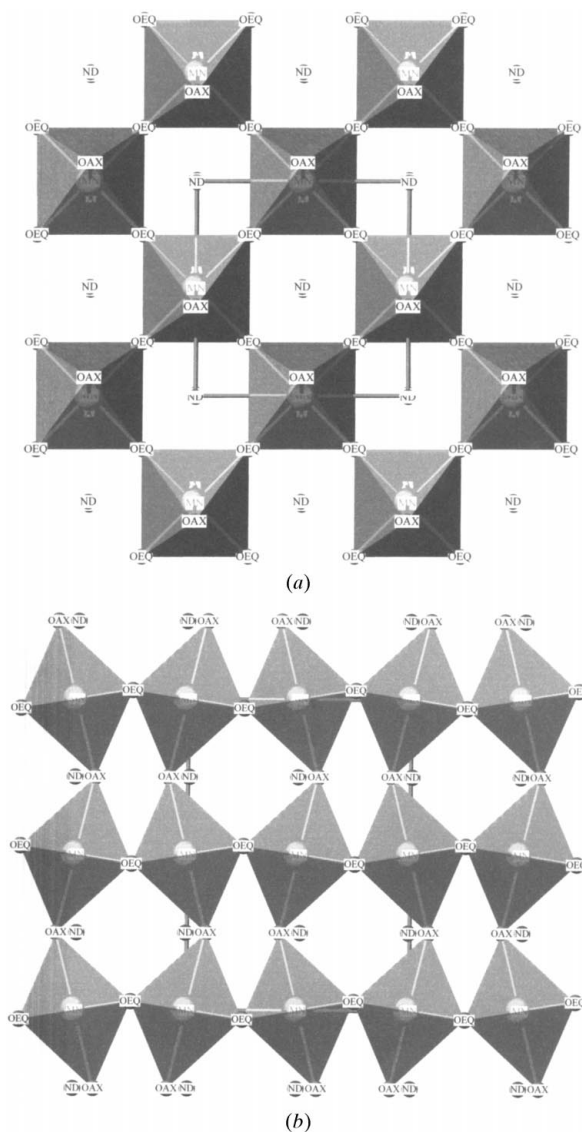


Figure 6
The relative arrangement of the MnO₆ octahedra at *T* = 200 K in (a) the *ac* plane and (b) the *bc* plane.

4. Conclusions

We have successfully characterized a complex phase transition in a doped manganate perovskite using a focused monochromatic synchrotron beam and an area detector to register the powder diffraction pattern. A total of 40 measurements were carried out in the temperature range 105–200 K, and a full Rietveld refinement was made on each data set. The exposure time per image was 10 s, leading to a total exposure time of less than 7 min for the complete data collection. Because of the readout and erase cycle of the MAR345 area detector and the thermal characteristics of the cryostream cooler, the entire experiment required about 2 h of beam time on an ESRF bending-magnet beamline. Using the experimental powder patterns determined in this fashion, we were able to make a full structural characterization of the phase transition. This included the observation of the coexistence of high- and low-temperature phases, the thermal hysteresis associated with the transition, and a detailed investigation of bond lengths and angles within the distorted MnO_6 clusters. Our results are in close agreement with earlier neutron diffraction data (Kawano *et al.*, 1997) and confirm the multiphase low-temperature behaviour observed recently by Woodward *et al.* (1999).

In our particular case the angular resolution achieved with the MAR345 image-plate detector was sufficient for the structural analysis. However, in many cases, for example with lower-symmetry materials, the resolution in this experiment would have been inadequate. It would not be difficult to modify the mechanical arrangement of the MAR345 to allow an off-axis mounting of the detector plate and an increased sample-to-detector distance. In this manner an improvement in the angular resolution by at least a factor of two would be quite feasible. However, the real breakthrough will come with the advent of a new generation of electronic detectors, with a large sensitive area, fast readout cycles and good pixel resolution. Detectors of this type are indeed under development in many synchrotron facilities (see *e.g.* Manolopoulos *et al.*, 1999; Fauth *et al.*, 2000), and their availability will revolutionize this type of materials study. The key to success in understanding complex systems such as the rare-earth manganates or cuprates is to measure the *entire* structural phase diagram of composition *versus* temperature for a variety of compounds. An investigation of this complexity would still, today, make prohibitive demands upon valuable synchrotron beam time. This will no longer be the case in

the near future, and materials scientists should be ready to exploit these developments.

The authors would like to thank F. Fauth for useful discussions. We are also grateful to P. Woodward and his co-authors for providing access to their results prior to publication. We would also like to thank the Swiss National Science Foundation for access to the facilities of the Swiss–Norwegian beamline and for financial support (PP). KDK acknowledges the financial support of the Research Council of Norway (project number 100822/431).

References

- Arulraj, A., Biswas, A., Raychaudhuri, A. K., Rao, C. N. R., Woodward, P. M., Vogt, T., Cox, D. E. & Cheetham, A. K. (1998). *Phys. Rev. B*, **57**, R8115–R8118.
- Caignaert, V., Millange, F., Hervieu, M., Suard, E. & Raveau, B. (1996). *Solid State Commun.* **99**, 173–177.
- Fauth, F., Bronnimann, C., Ahderset, H., Maehlum, G., Pattison, P. & Patterson, B. (2000). *Nucl. Instrum. Methods*, **439**, 138–146.
- Finger, L. W., Cox, D. E. & Jephcoat, A. P. (1994). *J. Appl. Cryst.* **27**, 892–900.
- Hammersley, A. (1999). *FIT2D*. Version 10.31. ESRF, Grenoble, France.
- Kawano, H., Kajimoto, R., Yoshizawa, H., Tomioka, Y., Kuwahara, H. & Tokura, Y. (1997). *Phys. Rev. Lett.* **78**, 4253–4256.
- Kuwahara, H., Okuda, T., Tomioka, Y., Asamitsu, A. & Tokura, Y. (1999). *Phys. Rev. Lett.* **82**, 4316–4319.
- Kuwahara, H., Tomioka, Y., Asamitsu, A., Moritomo, Y. & Tokura, Y. (1995). *Science*, **270**, 961–963.
- Laffez, P., van Tendeloo, G., Millange, F., Caignaert, V., Hervieu, M. & Raveau, B. (1996). *Mater. Res. Bull.* **31**, 905–911.
- Larson, A. C. & Von Dreele, R. B. (1987). Report LA-UR-86-784. Los Alamos National Laboratory, Los Alamos, NM, USA.
- Maezono, R., Ishihara, S. & Nagaosa, N. (1998). *Phys. Rev. B*, **57**, R13993–R13996.
- Manolopoulos, S., Bates, R., Bushnell-Wye, G., Campbell, M., Derbyshire, G., Farrow, R., Heijne, E., O’Shea, V., Raine, C. & Smith, K. M. (1999). *J. Synchrotron Rad.* **6**, 112–115.
- Moritomo, Y., Akimoto, T., Nakamura, A., Ohoyama, K. & Ohashi, M. (1998). *Phys. Rev. B*, **58**, 5544–5549.
- Radaelli, P. G., Cox, D. E., Marezio, M., Cheong, S.-W., Schiffer, P. E. & Ramirez, A. P. (1995). *Phys. Rev. Lett.* **75**, 4488–4491.
- Van Veenendaal, M. & Fedro, A. J. (1999). *Phys. Rev. B*, **59**, 1285–1289.
- Woodward, P. M., Cox, D. E., Vogt, T., Rao, C. N. R. & Cheetham, A. K. (1999). *Chem. Mater.* **11**, 3528–3538.
- Woodward, P. M., Vogt, T., Cox, D. E., Arulraj, A., Rao, C. N. R., Karen, P. & Cheetham, A. K. (1998). *Chem. Mater.* **10**, 3652–3665.